Results in Physics 52 (2023) 106737

Contents lists available at ScienceDirect

Results in Physics

journal homepage: www.elsevier.com/locate/rinp

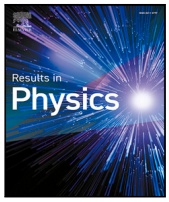

Complexity measurements for the thermal convection in a viscoelastic fluid saturated porous medium

L.M. Pérez [a,*,1], J.A. Vélez [b,c,1], M.N. Mahmud [d,1], R.M. Corona [e,f,1], S. Castillo-Sepúlveda [g,1], L. Pedraja-Rejas [h,1], R.M. Otxoa [i,c,1], H.L. Mancini [j,1], D. Laroze [k,1]

[a] Departamento de Física, FACI, Universidad de Tarapacá, Casilla 7D, Arica, Chile
[b] Departamento de Polímeros y Materiales Avanzados: Física, Química y Tecnología, Universidad del País Vasco, UPV/EHU, Paseo M. Lardizabal, 3, 20018 San Sebastián, Spain
[c] Donostia International Physics Center, 20018 San Sebastián, Spain
[d] Universiti Kuala Lumpur, Malaysian Institute of Chemical & Bioengineering Technology, 78000 Alor Gajah, Malaysia
[e] Departamento de Física, Universidad de Santiago de Chile, Avenida Ecuador 3493, Santiago, Chile
[f] Centro de Nanociencia y Nanotecnología, Avda. Libertador Bernardo O'Higgins, 3363 Estación Central, Chile
[g] Departamento de Ingeniería, Universidad Autónoma de Chile, Avenida Pedro de Valdivia 425, Providencia, Chile
[h] Departamento de Ingeniería Industrial y de Sistemas, Universidad de Tarapacá, Casilla 7D, Arica, Chile
[i] Hitachi Cambridge Laboratory, J. J. Thomson Avenue, Cambridge CB3 0HE, United Kingdom
[j] Departamento de Física y Matemática Aplicada, Universidad de Navarra, 31080, Pamplona, Spain
[k] Instituto de Alta Investigación, Universidad de Tarapacá, Casilla 7D, Arica, Chile

ARTICLE INFO

Keywords:
LMC complexity
Lyapunov exponents
Generalized Lorenz models

ABSTRACT

Measuring complexity statistical indicators is a key method to analyze and characterize dynamical systems. In this work, we perform a comparative analysis among the López-Ruiz, Mancini & Calbet complexity indicator and the largest Lyapunov exponent for the convection problem of a viscoelastic fluid in a porous medium with feedback control based in an Oldroyd carrier liquid through a four-dimensional generalized Lorenz system. With both indicators can be distinguished from chaotic to periodic states. We perform intensive numerical simulations with 4×10^6 in the space parameters, finding good agreement between them, such that difference is close to 2%. We have also detected that the computing time is much faster in the case of complexity indicator than for Lyapunov exponents. Finally, we have also studied the effect of the initial conditions in the coexistence states, encountering multistability.

Introduction

The concept of entropy plays a crucial role in macroscopic systems in order to determine the condition for thermodynamic equilibrium. The probability distribution of a restricted system to the accessible states is given by the principle of maximum entropy inference [1]. The typical macroscopic magnitudes as well as the relationship among them can be obtained by standard statistical mechanics techniques from the probability distribution function. In addition, in equilibrium, the concept of entropy can be connected to the amount of information that is accessible in a system [2]. A similar scheme could be extrapolated to systems far from equilibrium. However, under these circumstances, it is more difficult to establish a method to find the probability distribution function or to figure out the relevant magnitudes, which could allow us to predict the system behavior. This is one of the main topics of nonequilibrium statistical mechanics [3–5]. In this context, the first approach to understand the dynamic states of non-equilibrium systems from a statistical perspective was defined in the Ref. [6], which is usually known as the López-Ruiz, Mancini & Calbet (LMC) complexity indicator. The main assumption was to define a dynamical system for which the complexity is obtained as the product of two measures: the information and disequilibrium. Such information is quantified by the Shannon entropy and the disequilibrium is a measure of the distance from the equiprobable distribution of the accessible states of a system. Hence, this product becomes zero for both: ordered and random systems. Interestingly, it can be interpreted as some sort of distance among the equiprobable states accessible by the system. Subsequently, it is stressed here that the complexity measure does not depend only on the concept of information (which are maximal and minimal for

* Corresponding author.
E-mail address: lperez@academicos.uta.cl (L.M. Pérez).
[1] All the authors contributed equally to this work.

https://doi.org/10.1016/j.rinp.2023.106737
Received 13 March 2023; Received in revised form 23 June 2023; Accepted 7 July 2023
Available online 13 July 2023

the above mentioned system). The prototype model used to test the theory was the logistic map, which is, undoubtedly, one of the most used models to study complex systems. Moreover, it was shown that the sum of the positive Lyapunov exponents is equal to the Kolmogorov–Sinai entropy [7] and that the upper bound of the Lyapunov exponents can be obtained using the permutation Shannon entropy [8]. Therefore, these studies provide a tangible possibility of being able to quantify the emergence of chaos through the complexity method. Furthermore, it has been possible to distinguish chaotic series from a noisy one [9]. Discussions, generalizations and applications of the complexity's concept can be found in Refs. [10–32]. For instance, this complexity indicator has been used to study nonequilibrium isolated system [13], to analyze the dynamical behavior of anti-ferromagnet [15], to examine the earthquake phenomenon [17], or to investigate astronomical data [22]. Generalization of LMC complexity to analyze chaotic states has also been performed [23,24] or examined the fluid motion [26] and financial time series [28], as well. Even more, interesting recent studies on complexity have been performed in electric circuits from experimental and theoretical points of view [33,34]. One of them can have an application for image encryption [33]. Apart from the complexity measurements, the authors have found multi-stable states with a new method to find them [34].

On the other hand, the study of convection in viscoelastic fluids has gained a lot of interest due to its technological applications as well as because its richness from a pure mathematical perspective. The state of the art is exposed in Refs. [35–44]. One of the central points has been the effect of viscoelasticity in the emergence of different types of instabilities through variants of the Lorenz model [45–47], which was motived by the experimental results of Kolonder who found oscillatory convective instability in viscoelastic carrier liquids [48]. It has also been studied how the effect of a porous medium in this type of fluid modifies the convection thresholds [49,50]. In particular, it has been shown that it is possible to obtain chaotic states in viscoelastic fluids in a porous medium [51,52]. In addition, it has been shown that using a feedback control system in fluids it is possible to induce a slow down the instability or taming chaos [53,54]. In fact, it is possible to stabilize the chaos using a time-delay control [55]. Recently, the dynamical behaviors of convective rolls with feedback control for an Oldroyd fluid have been characterized, finding intricate topological structures of regular states embedded in chaotic domains in the two-dimensional phase diagram of the largest Lyapunov exponent in the parameter space [56]. The analysis was performed for fixed porosity, then it opens the door to extend the examination of dynamics when the porosity and the other control parameters are modified.

In this work, we perform a comparative analysis among the LMC complexity indicator and the largest Lyapunov exponent for the problem of convection of a viscoelastic fluid in a porous medium with feedback control based on the Oldroyd model. For this study, we use the four-dimensional generalized Lorenz system [56], which is derived from the equations of hydrodynamics. From the physical viewpoint, we will focus on the effects of porosity and the feedback control parameter, as well as viscoelasticity, which have not been previously studied. This analysis enlarges the understanding of the influence of the viscoelastic properties on convection problems in porous media. In particular, we perform intensive numerical simulations for both indicators, performing several two-dimensional diagrams in the parameter space, each of them with 4×10^6 points. We will show that there is a coincidence of more than 98% between both dynamic indicators. The amount of simulations ensures that the comparison of the methods has statistical significance. Also, to perform further analysis of the dynamical system, we compute the isospike diagrams to understand the periodicity of the regular states. Finally, we compute the coexistence of attractors and their corresponding basin of attractors for a specific set of parameters. The manuscript is arranged as follows: In Section "Theoretical model: generalized Lorenz system", the theoretical model for the generalized Lorenz model is presented. In Section "Simulations", the dynamical indicators and the numerical results are shown and analyzed. Finally, the conclusions are given in Section "Final remarks".

Theoretical model: generalized Lorenz system

Let us consider a two-dimensional Oldroyd viscoelastic fluid in a saturated porous medium heated from below and cooled from above subject to the gravity field, such that the sensors and actuators to have feedback control are placed at the top and bottom heated plates of the fluid-saturated porous layer, respectively. This model is fully described by a nonlinear coupled system of partial differential equations for the velocity and thermal fields as well as for the stress tensor. If one considers a large container, a simplified model that describes the instability of rolls can be derived using a truncated Galerkin expansion [57,58], which produces a set of nonlinear ordinary differential equations. In this scenario, the corresponding modified Lorenz equations are given by [56]:

$$\dot{X} = W, \tag{1}$$

$$\dot{Y} = \bar{C}_g r X - Y - \left(\bar{C}_g r - 1\right) X Z, \tag{2}$$

$$\dot{Z} = 4\gamma(XY - Z), \tag{3}$$

$$\begin{aligned} \dot{W} =& \sigma \left[\left(\bar{C}_g r - \frac{1}{\Gamma}\right) X + \bar{\Gamma} Y\right] \\ & - \sigma \left[\left(\bar{C}_g r - 1\right) XZ - \bar{\Lambda} W\right], \end{aligned} \tag{4}$$

where the dot $(\cdot)$ denotes the time derivative $\mathrm{d}()/\mathrm{d}\tau$. From the physical point of view, $\{X, W\}$ are related to the velocity field, whereas $\{Y, Z\}$ are related to the temperature field. Besides, for convenience, we have used the following notation: $\bar{C}_g = (10 - C_g)/10$, $\bar{\Lambda} = (\Lambda + (\sigma\Gamma)^{-1})$, and $\bar{\Gamma} = -1 + 1/\Gamma$, such that C_g is feedback control parameter, while Λ and Γ are the retardation number and the Deborah number, respectively. Both parameters account for the effect of viscoelasticity [45]. Also, the parameters σ and r are the normalized Vadasz number and the Darcy–Rayleigh number, respectively. We remark that σ represents the effect of porosity on the flow in a porous medium, while r accounts for the ratio of the buoyancy force to the diffusive resistance of the porous media, which is also called the Rayleigh number for a porous medium [51]. Finally, γ is a geometric parameter.

Let us remark that the previous dynamical systems, $\dot{\mathbf{X}} = \mathbf{F}(\mathbf{X})$, is a generalization of the Lorenz equations, which considers the viscoelasticity and the feedback control. Besides, note that, the uncontrolled system ($C_g = 0$) was studied in Ref. [51], and the Newtonian limit ($\Lambda \to 1$ and $\Gamma \to 0$) was previously analyzed in Ref. [59]. Let us comment on this limit, the system can be reduced to the standard Lorenz model [57], which from a mechanical point of view, can be interpreted as the normal form of a quasi-reversible system [60]. Also, note that the set of uniform solutions, $\{\mathbf{X}_0\}$, are obtained from $\mathbf{F}(\mathbf{X}_0) = \mathbf{0}$; and their linear stability $\det[\mathbf{J} - \mathbf{I}\zeta] = 0$, where ζ are the eigenvalue and $\mathbf{J}$ is the Jacobian matrix evaluated at $\mathbf{X}_0$. In the next section, we will perform intensive numerical simulations.

Simulations

In this section the dynamical behavior of the system (1)–(4) is analyzed. The numerical method to solve the equations is the classical fourth order Runge–Kutta method with a fixed time step of $\Delta\tau = 5 \times 10^{-3}$. In all simulations, we discard a time window of 8×10^5 time steps, to avoid transitory states. Other values of $\Delta\tau$ have been employed to check the accuracy, yielding no significant changes.

Indicators

We characterized the dynamical states as a function of the parameters using Lyapunov exponents, LMC complexity indicator, bifurcation diagrams and direct time-series analysis, like the isospike diagrams that reveals how the periodicity changes when the parameters are tuned.

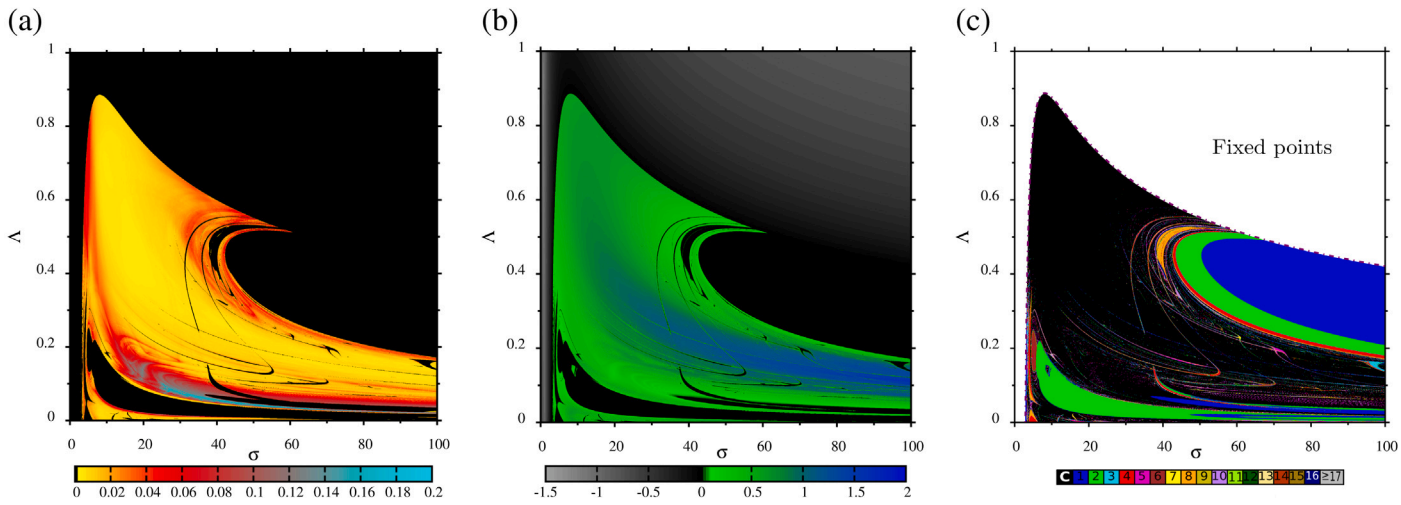

Fig. 1. Phase diagrams in color code a function of both Λ and σ for the LMC complexity indicator (a), the LLE (b) and the Isospike of the Z component (c). The fixed parameters are $\Gamma = 1.0$, $r = 55.0$ $\gamma = 0.5$, and $C_g = 7.0$. (For interpretation of the references to color in this figure legend, the reader is referred to the web version of this article.)

The bifurcation diagrams are computed by counting the values of the local maximum of the time-series of a specific variable [58].

On the other hand, for a M-dimensional dynamical system, the Lyapunov exponents measure the sensibility to the initial conditions [61–63]. They are commonly denoted by the symbols λ_j with $j = (1, \ldots, M)$, and ordered in a decreasing form, such as the largest Lyapunov exponent (LLE), denoted by λ_1. The exponential divergence of two initially close trajectories, which is characteristic for chaotic dynamics, is detected when positive LLE are found. If the LLE is negative the state is stationary, whereas when LLE is zero the system exhibits a regular state, which can be periodic or quasi-periodic. Besides, if there are two positive Lyapunov exponents, the system exhibits a hyper-chaotic state [64–67]. If both the largest and the second largest Lyapunov exponents are zero, the system holds a quasi-periodic state. In addition, with the whole Lyapunov spectrum, one can calculate the Kaplan–Yorke dimension, D_{KY}. This indicator gives the attractor's dimension and is a valuable tool in a dynamical system with a large number of variables to distinguish from low dimensional chaos to spatiotemporal one. The Kaplan–Yorke dimension can be computed as:

$$D_{KY} = k + \frac{1}{|\lambda_{k+1}|}\sum_{i=1}^{k}\lambda_i, \tag{5}$$

such that k is the largest integer for which $\sum_{i=1}^{k}\lambda_i \geqslant 0$. This definition implies that if there is only one positive Lyapunov exponent positive and all the rest with negative values, $D_{KY} > 1$, whereas if there is one positive and one zero Lyapunov exponent with all the rest negatives, $D_{KY} > 2$. Besides, if all Lyapunov exponents are negative, $D_{KY} = 0$. Let us remark that, the Lyapunov spectrum technique has been well established in several dynamical systems [62,63,68–71] and intensive numerical simulations can be found in Refs. [72–88]. Here, we apply the Gram–Schmidt orthogonalization procedure periodically (here, we renormalize every $\tau = 1$ unit). The integration for determining the Lyapunov exponents has been prolonged for a time of $\tau = 2^{15}$. These very long simulations allow minimizing the error on the computed exponents. The typical standard error on the maximum Lyapunov exponent was approximately equal to 9×10^{-5}.

To obtain the isospike diagrams [89,90], that is, to find the number of peaks per period of the oscillations, we first calculate the Lyapunov exponents to discard the chaotic states, and perform the integrations for 3×10^5 time steps, recording the maxima (or minima) of the time series of each component of the vector field, $\mathbf{X}(\tau)$, and check whether the peaks are repeated or not. Applications of isospike technique can be found in Refs. [91–104].

Now, let us present a small discussion on the statistical description of the system by using the LMC complexity indicator, $\mathscr{C}_{LMC}$, which was originally derived in Ref. [6]. For this purpose, let $\zeta = \zeta(t)$ be a time series with N accessible states when it is observed from a certain scale. We will call it as N-system. Eeach state corresponds to a certain probability, then there is a set of N probability functions, $\{p_1, p_2, \ldots, p_N\}$, under the condition $\sum_{i=1}^{N} p_i = 1$, such that $p_i \neq 0$ for $\forall i$. At this level, all fundamental physical laws would incorporate the probability distribution for accessible states associated to the time series. To compute $\mathscr{C}_{LMC}$, it is needed to convert the N-system into a binary system with values 1 and 0. To do that, we employ the following algorithm:

1.- The expected value, $\langle\zeta\rangle$ is calculated from the time series.

2.- The time series is normalized in the range $(0, 1)$ by

$$\hat{\zeta} = \frac{|\zeta - \langle\zeta\rangle|}{\max(|\zeta - \langle\zeta\rangle|)}. \tag{6}$$

3.- The set of local maxima from the normalized time series is calculated, $\{\hat{\zeta}_{m,1}, \ldots, \hat{\zeta}_{m,P}\}$, and from these maxima it is taken its corresponding mean value $\hat{\Sigma}$.

4.- The previous set is codified in binary code as: 0 if $\hat{\zeta}_{m,j} < \hat{\Sigma}$ and 1 if $\hat{\zeta}_{m,j} > \hat{\Sigma}$.

5.- For this binary code a pattern is identified from an array with a specific n_s. This array is selected and it is consider a micro-state.

6.- Now, the system has been converted into chain of binary numbers with an integer number of micro-state. The number of all micro-states is N.

7.- The histogram of the integer numbers that arise which correspond to the accessible micro-states, p_i, of the system is calculated.

8.- The steps 5–7 are repeated several times to ensure that the optimal n_s has been obtained.

9.- The information entropy of the system, $\mathscr{H}$, is calculated via

$$\mathscr{H} = -K\sum_{i=1}^{N} p_i \log p_i, \tag{7}$$

where K is a positive constant.

10.- The disequilibrium function, $\mathscr{D}$, is calculated through

$$\mathscr{D} = \sum_{i=1}^{N}(p_i - 1/N)^2. \tag{8}$$

11.- Finally, it is calculated the LMC complexity indicator, $\mathscr{C}_{LMC}$, as the product between the entropy and disequilibrium function:

$$\mathscr{C}_{LMC} = \mathscr{H} \times \mathscr{D}. \tag{9}$$

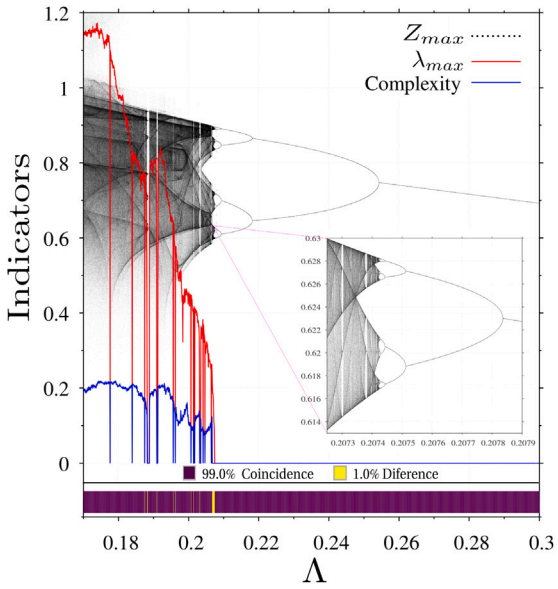

Fig. 2. Bifurcation diagram of the Z component (black dots), Largest Lyapunov exponent λ_{max} (red line) and Complexity indicator $\bar{\mathscr{C}}$ (blue line), as a function of Λ at $\sigma = 80$. The other fixed parameters are the same as in Fig. 1. (For interpretation of the references to color in this figure legend, the reader is referred to the web version of this article.)

We remark that for this definition of entropy, we can infer that for a periodic and stationary states $\mathscr{H} = 0$, therefore, as there is only one single state, p. Due to $0 \leqslant \mathscr{D} \leqslant N/(N-1)$ and to $0 \leqslant \mathscr{H} \leqslant K$ imply that $\mathscr{C}_{LMC} \geqslant 0$. Therefore, in deterministic dynamical systems, $\mathscr{C}_{LMC}$ for stationary and periodic states is zero ($\mathscr{C}_{LMC} = 0$), while for chaotic states is greater than zero, $\mathscr{C}_{LMC} > 0$.

For the present problem, the LMC complexity indicator is computed for each component of the vector field $\mathbf{X}$, and then we take the average:

$$\bar{\mathscr{C}} = \frac{\mathscr{C}_{LMC,X} + \mathscr{C}_{LMC,Y} + \mathscr{C}_{LMC,Z} + \mathscr{C}_{LMC,W}}{4} \tag{10}$$

Also, let us comment that to calculate micro-states array, we have used $n_s = 12$. We have explored other values of n_s and we found that this one was optimal value. In this context, we would also remark that the same value of n_s has been used for the original LMC work and in other dynamical systems as well [6,9,13,16]. From the numerical point of view, to ensure to have a good statistic, we have used after the transient a time series with 4×10^6 time steps.

In the next subsections, we present numerical results of these dynamical indicators and make a comparison of them. Due to the large numbers of parameters, we fix $r = 55.0$, $\Gamma = 1.0$ and $\gamma = 0.5$, while the parameters σ, Λ, as well as C_g will be varied. These parameters account the effect of the porosity, the viscoelasticity and the feedback control, respectively. In several simulations, two parameters are simultaneously varied, creating two-dimensional phase diagrams of the different dynamical indicators. The resolution of each diagram is 2000 × 2000 in the parameter space. Finally, let us comment that for most of the simulations, we fix the initial conditions at $\mathbf{X}(\tau = 0) = (0.9, 0.9, 0.9, 0.1)$, except in the last subsection in which the influence of initial conditions is examined.

Effects of the porosity and viscoelasticity

Fig. 1 shows color code two-dimensional phase diagrams as a function of Λ and σ for the largest Lyapunov exponent, λ_{max}, complexity indicator, $\bar{\mathscr{C}}$ as well as for the isospikes. Let us remark that when λ_{max} is zero or lower than zero the system exhibits regular states, which are (quasi)-periodic or stationary states, respectively. In these cases, one always has that $\mathscr{C}_{LMC} = 0$, because it does not discriminate among periodic and fixed point states because in both cases it is zero. We can observe that critical value of Λ as a function σ from the linear stability analysis follows the relationship $\Lambda_H(\sigma) = -a/\sigma^2 + b/\sigma^{1/3}$ where $(a, b) = (11.0054, 2.06637)$. Bellow the critical curve, the states are mostly chaotic. We can distinguish some internal structure where there are regular pattern embedded in chaotic domains. Besides, when it is compared the results from the panel (a) and (b) of Fig. 1, one can find a difference near to 2% between both dynamical indicators. This is an excellent agreement. From the third panel, in which the isospikes are shown, it is easy to distinguish the types of regular states. The white area corresponds to fixed points, while the discrete color bar provides the value of the periodicity, being black color chaos. We can observe that this diagram presents more information. It shows clearly the limit between the combined chaotic states, limit cycles and fixed point states (white region from panel c). From the physical point of view, in Fig. 1, we can notice that we will only have stationary convection rolls in the zone higher than the Λ_H curve. It also means that this regime continues for fluids closer to Newtonian behavior (near to $\Lambda \gtrsim 0.9$), regardless of the fluid's porosity (any value of the Vadasz number). For intermediate Vadasz values ($10 \lesssim \sigma \lesssim 40$), the convection rolls are chaotic or have high periodicities for a large spectrum of Λ values. Indeed, it is shown that viscoelasticity can tame chaos, having periodic solutions in a regime close to the Maxwellian fluid ($\Lambda \approx 0$). We also note that there is an engaging zone at high porosity ($\sigma \gtrsim 55$) bellow Λ_H curve, the rolls undergo a bifurcation from stationary to periodic states with period one. In fact, for instance, if one fixes $\sigma = 80$ after the period-one regime by reducing the elastic coefficient values, a cascade of bifurcations is produced before reaching chaos.

Fig. 2 shows λ_{max}, the complexity indicator $\bar{\mathscr{C}}$ and a bifurcation diagram of the Z component as a function of Λ at $\sigma = 80$. This is a line of the complexity indicator phase diagram 1 at $\sigma = 80$ with a greater resolution in Λ, with 2×10^4 lattice points. We can observe that the bifurcation diagram shows an extended view of the unfolding periodic bifurcations as Λ increases, from chaos, passing from several multi-periodic states to period one solution. We can also verify that the λ_{max} and $\bar{\mathscr{C}}$ has an excellent agreement in the whole range of the bifurcation parameter. In fact, the inferior part of Fig. 2 shows a barcode that represents the difference between $\bar{\mathscr{C}}$ and λ_{max} from which we found that the percentage difference is only 1%. Let us remark that the differences are mainly occurred in the transition among periodic and chaotic states, in which the numerical sensibility of the indicators is crucial.

Fig. 3 displays three specific examples of the dynamical behaviors, one chaotic and two periodic states taken form previous simulations for three fixed values of Λ. In particular, we choose $\Lambda = (0.2, 0.21, 0.24)$, respectively. The top panels show the time series of the Z component, while the bottom ones display the three dimensional parametric plot of (X, Y, Z) components in the phase space. Panel (a) corresponds to a chaotic state, where a similar Lorenz attractor is obtained, whereas panel (b) and (c) show periodic cases. We can observe that for the periodic cases have four- and two-isospike, respectively. In these cases, the values of complexity are $\bar{\mathscr{C}} = (0.07, 0, 0)$, as we expected the not zero value of $\bar{\mathscr{C}}$ is for the chaotic state.

Effects of the porosity and feedback control

Now, let us focus on the effects of porosity and feedback control in detail. Fig. 4 shows the phase diagrams in color code of the complexity indicator, $\bar{\mathscr{C}}$, the isospike diagram of the Z component, and the distribution of the periods calculated using fast Fourier transform of all components as a function of normalized Vadasz number, σ, and the feedback control parameter C_g. From panel (a) we can distinguish between chaotic ($\bar{\mathscr{C}} > 0$) and regular ($\bar{\mathscr{C}} = 0$) states. Indeed, we observe that the chaos appears for $\sigma \gtrsim 4$ and $C_g \lesssim 8.2$. Typical shrimp patterns from the different periodic islands can be observed in this

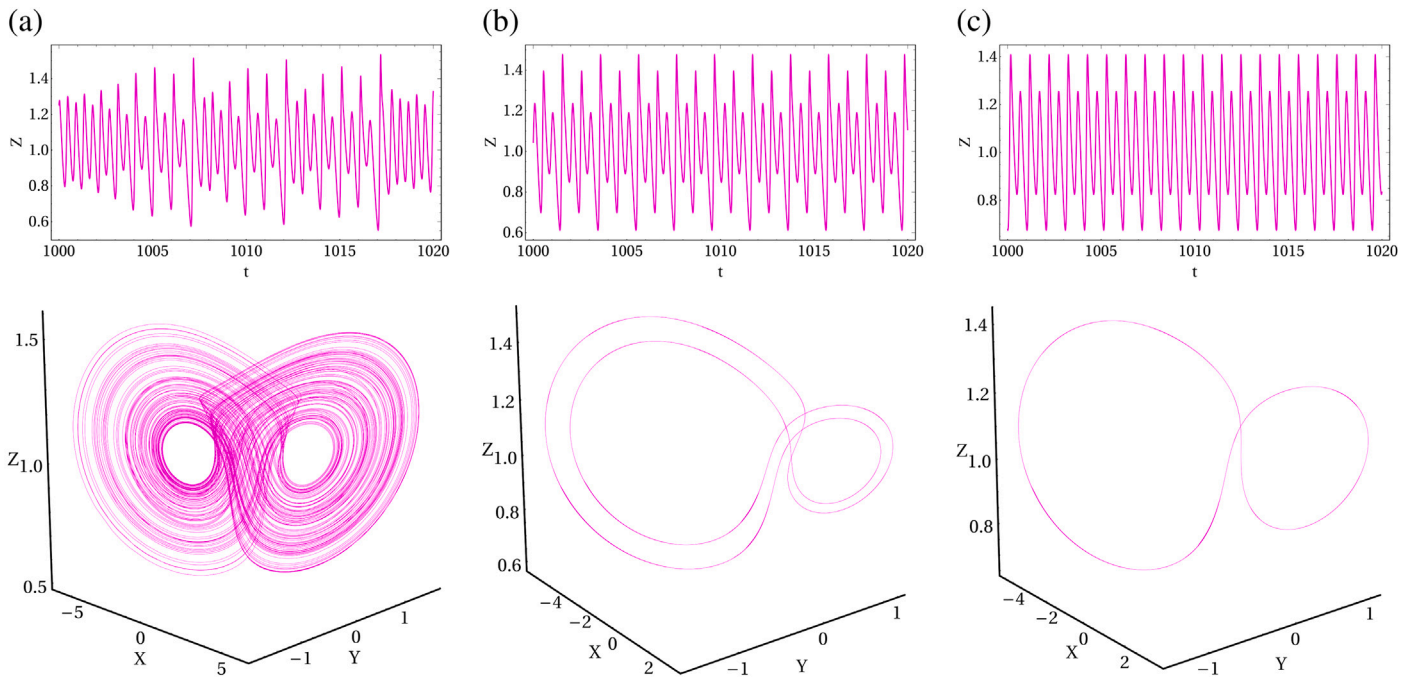

Fig. 3. Time series of the Z component and three dimensional phase diagram of the components (X, Y, Z) for (a) chaotic state, (b) a periodic state with 4-isospike and (c) periodic state with 2-isospike. The fixed values of Λ are $\Lambda = (0.2, 0.21, 0.24)$, respectively. The other fixed parameters are the same as for Fig. 2.

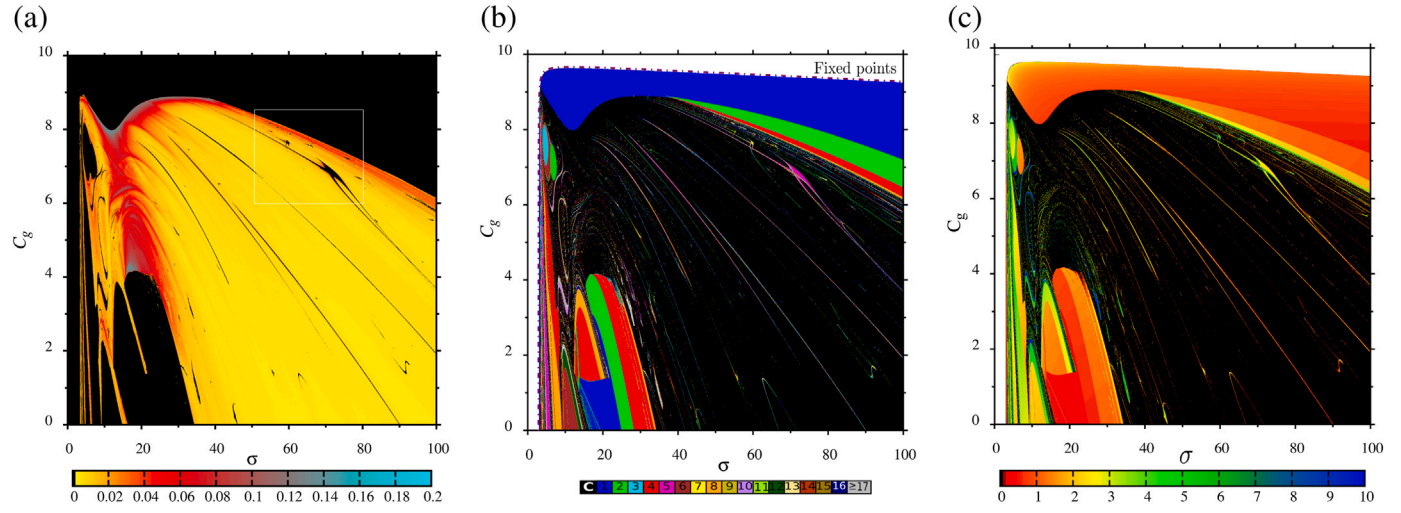

Fig. 4. Phase diagrams in color code a as function of both C_g and σ for LMC complexity indicator (a), isospike diagram of the Z component (b) and period distribution (c). The resolution in each panel is $\Delta C_g = 0.005$ and $\Delta\sigma = 0.05$. The fixed parameters are: $\Gamma = 1.0$, $\Lambda = 0.20$, $r = 55.0$ and $\gamma = 0.5$. (For interpretation of the references to color in this figure legend, the reader is referred to the web version of this article.)

region. Panel (b) provides information to discriminate between fixed point states and periodic states within the number of peaks in the time series of each periodic state. In this region, typical shrimp patterns from the different periodic islands can be observed. Also, we can observe that for $\sigma > 40$, a route towards chaos through the doubling of the bifurcation period as C_g decreases. The same happens for $\sigma \in (20, 40)$ for $C_g < 4$. Finally, panel (c) displays the phase diagram of the period distribution in arbitrary units. In the color bar, we have chosen black and white for chaotic and fixed points in which the period has no meaning. We can notice that for small values of isospike, the period is small too, and it increases when the values of isospike increase, given a strong correlation among both diagrams. From the physical point of view, we have chosen a parameter region that represents a standard Oldroyd viscoelastic fluid ($\Gamma = 1.0$ and $\Lambda = 0.2$) with a high-temperature gradient since the Darcy–Rayleigh number is $r = 55.0$. We note that above the $C_{g,H}(\sigma) = 10.588/\sigma^{0.029} - 15/\sigma^2$ curve, all states are stationary convection rolls. Just after crossing the Hopf bifurcation, for high values of the feedback control parameter, the rolls bifurcate to periodic states with period-one, almost independent of porosity. Then in the intermediate zone of both parameters, there are multiple transitions among different states. On the other hand, we can also observe that when the feedback control parameter is less than half the maximum value, the chaotic states practically dominate for high and intermediate porosities.

Fig. 5 shows a zoom of the square in panel (a) of Fig. 4. It reveals a successive periodic structure pattern with shrimp form, which appear linearly ordered while their size increases as σ increases and C_g diminishes. Other smaller periodic structures also occur, but to reveal the shape, iterative zooms are needed. Panel b presents a bifurcation diagram of the maximum values of Z, $\bar{\mathscr{C}}$ and λ_{max} as a function of the

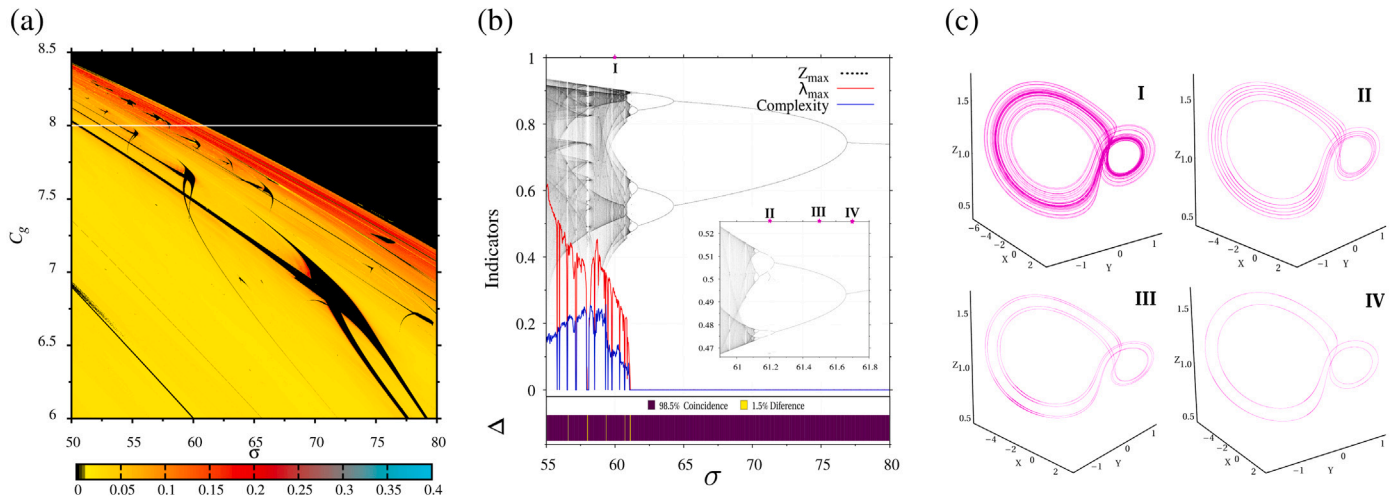

Fig. 5. Panel (a) shows an extended view of the Complexity phase diagram of Fig. 4a. Panel (b) corresponds to the bifurcation diagram, λ_{max} and the complexity corresponding to the solid line marked in panel (a). Panel (c) corresponds 3D plots in the phase space of the (X, Y, Z) components for the following fixed values: **(I)** $\sigma = 60.0$, **(II)** $\sigma = 61.2$, **(III)** $\sigma = 61.5$ and **(VI)** $\sigma = 61.7$. All the other fixed parameters are the same as in the Fig. 4.

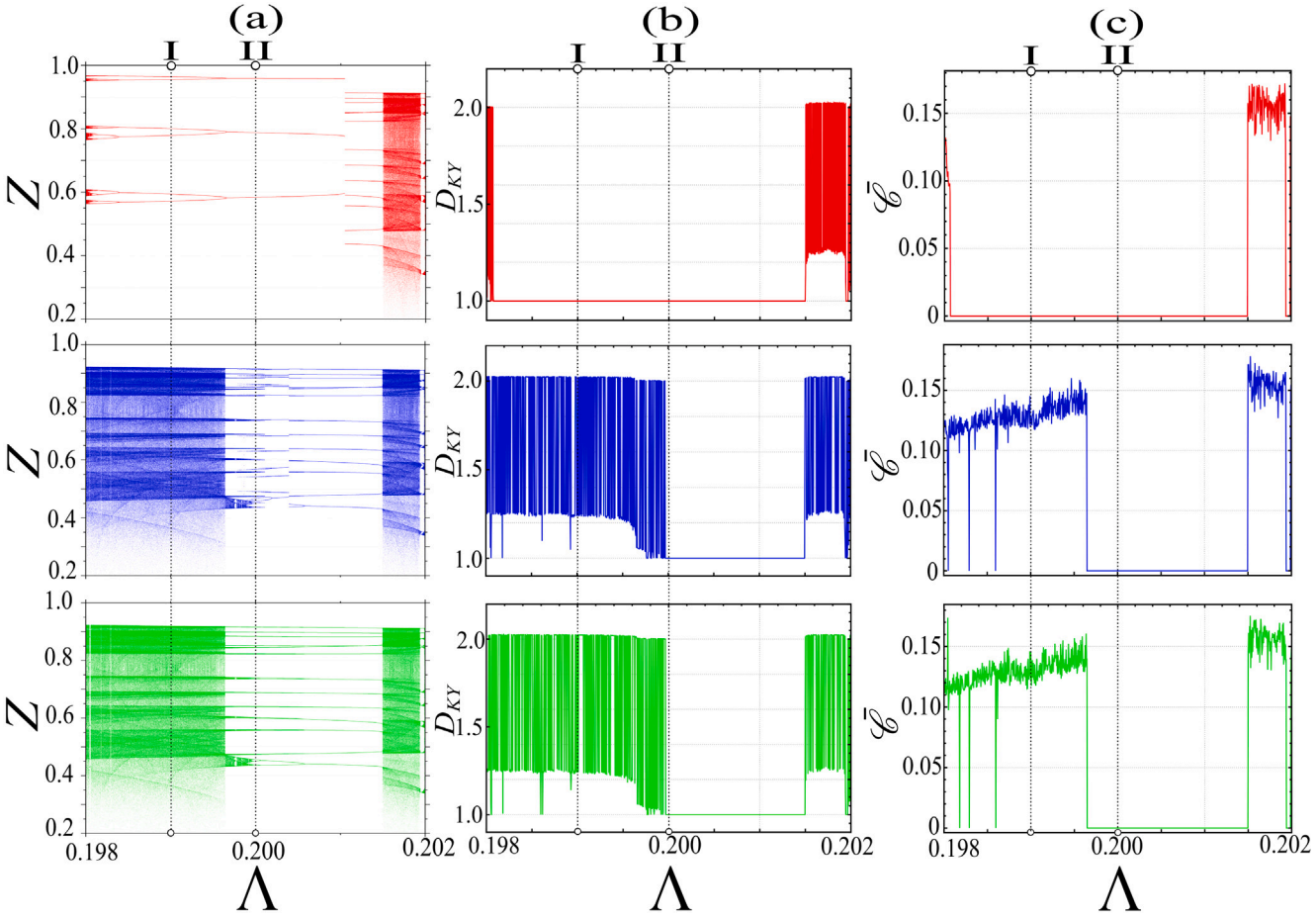

Fig. 6. (a) Bifurcation diagram of the Z component, (b) Kaplan–Yorke Dimension, D_{KY}, and (c) Complexity indicator $\bar{\mathscr{C}}$, as a function of Λ starting with three different initial conditions. The three panels for each indicator represent different initial conditions, which are colored to identify by red (top), blue (intermediate) and green (bottom), respectively. The fixed parameters are: $\Gamma = 1.0$, $r = 55.0$, $\sigma = 58.0$, $\gamma = 0.5$ and $C_g = 8.0$. (For interpretation of the references to color in this figure legend, the reader is referred to the web version of this article.)

parameter σ for a fixed value of the feedback control, $C_g = 8.0$. We observe coincidence among the three indicators. In the chaotic regions where $\lambda_{max} > 0$, the bifurcation diagram shows dispersion associated with the maxima from the time series. We present a time window series that adjust very well to the indicators λ_{max} and $\bar{\mathscr{C}}$. The bifurcation diagram shows a route to chaos through the doubling of the period as σ decreases. In the lower part of panel (b) of Fig. 5, we show a bar that marks the distinct behavioral dynamics of the complexity $\bar{\mathscr{C}}$ and λ_{max}. Note that the differences are easily observed at the frontiers between periodic and chaotic states with a percentage difference of less

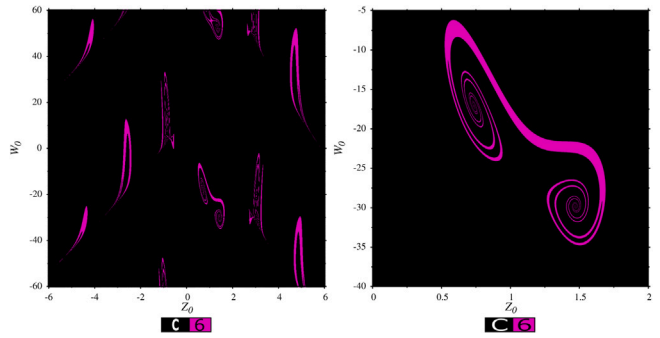

Fig. 7. Isospike diagram of the Z component as a function of the initial condition W_0 and Z_0 at $(X_0, Y_0) = (-34, 1.6)$. The fixed parameters are the same as in Fig. 6 at $\Lambda = 0.199$.

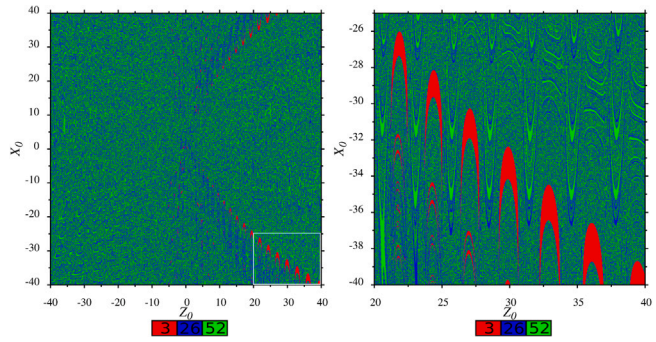

Fig. 8. Isospike diagram of the Z component as a function of the initial condition X_0 and Z_0 at $(Y_0, W_0) = (0.9, 0.1)$. The fixed parameters are the same as in Fig. 6 at $\Lambda = 0.2$.

than 1.5%, which is a slight difference. Lastly, panel (c) shows four particular cases in the phase space for the X, Y, and Z components' behaviors. The selected parameters are marked in the Fig. 5b. For the case, **(I)** in $\sigma = 60.0$ corresponds to a chaotic state with a $\lambda_{max} = 0.29$, where once again a Lorenz-like attractor is obtained. Cases **(II)**, **(III)**, and **(IV)** correspond to a state with 12, 6, 4, and 2 isospike, where a periodic doubling sequence is lost. The diagram shows a discontinuity in the branches when $\sigma = 61.2$ due to the system presenting dual stability.

Effects of the initial conditions

Usually nonlinear systems, like generalized Lorenz model, can have multistable solutions, some of them are hidden attractors [34,62,86,97,100,105–111]. For instance, it has been recently found the coexistence of several attractors in a hyper-chaotic system [34]. Furthermore, in the Lorenz model has been found hidden attractors that coexists with other well known solutions [111]. Therefore, in this last subsection we study the effect of the initial conditions in order to explore the possibility of coexistence of different attractors in our dynamical system.

Panel (a) of Fig. 6 shows the bifurcation diagram of the Z component, panel (b) the Kaplan–Yorke dimension, D_{KY}, and panel (c) the complexity indicator $\bar{\mathscr{C}}$, as a function of Λ, starting with three different initial conditions. We have performed the continuation processes for each of them. Also, there are sub-panels with different colors per condition. In particular, we have taken the values of these initial conditions at the beginning of the diagram as follows: $\mathbf{X}^{(r)}(\tau = 0) = (-4.65, -0.40, 0.63, -0.30)$ (red), $\mathbf{X}^{(b)}(\tau = 0) = (-3.27, -0.15, 1.49, 46.7)$ (blue) and $\mathbf{X}^{(g)}(\tau = 0) = (2.37, 0.85, 0.94, 9.01)$ (green). We can definitely observe that there are multistability among plenty of different states. We can also see that the transition from a regular to a chaotic state differs depending on the branch. However, all branches converge into the same periodic state in the range $\Lambda \in (0.199956, 0.201496)$ and then suddenly bifurcate to chaos at $\Lambda = 0.201498$. There are more similarities between the blue and green branches in the range $\Lambda \in (0.199644, 0.198058)$, in which both exhibit only chaotic states, whereas the red one displays only periodic states. On the other hand, we can notice that the three indicators show good agreement among them.

Now, let us analyze in more detail the basin of attractions of different states for two specific sets of parameters. In particular, we will focus on two cases, one in which there is coexistence of chaotic and periodic states and the other in which there is coexistence only among regular states. These sets are depicted as **I** and **II** in the bifurcation diagrams, respectively. Panel (a) of Fig. 7 shows the two-dimensional isospike diagram of the Z-component as a function of the values of the initial conditions W_0 and Z_0 for fixed (X_0, Y_0). In this wide range of values, there are only two types of solutions, chaotic and periodic, with a 6-spike per period. The regular regions form quite fascinating patterns. In particular, we can observe a double spiral pattern, as it can be seen in the zoom exposed in panel (b) of the same figure. Finally, panel (a) of Fig. 8 displays the two-dimensional isospike diagram of the Z-component as a function of the values of the initial conditions X_0 and Z_0 for fixed (Y_0, W_0). This diagram corresponds to the parameter set **II**. Here, we can observe that there is coexistence among three regular states with 3-, 26- and 52-isospike, repetitively. It can be seen that for negative values of Z_0, there is no apparent order, such that the least predominant state is the 3-isospike. For positive values of Z_0, an order emerges. A zoom is shown in panel (b) to notice better the pattern formation, where we see boomerang-like structures for the three types of periodic states.

Final remarks

In this manuscript, we have performed a comparative analysis of different dynamical indicators in the problem of the convection of a viscoelastic fluid in a porous medium with a control feedback mechanism. The system has been characterized by a set of four coupled nonlinear differential equations. We have focused mainly on the characterization by the largest Lyapunov exponent and LMC complexity indicator. We have carried out intensive numerical simulations in the space parameter with resolutions in the phase diagrams of 2000×2000. Making a comparative analysis, we have been able to conclude that there is only a discrepancy of less than 2% between both indicators. This result is noteworthy because with $\mathscr{C}_{LMC}$, it is only necessary to work with the time series, which significantly reduces the computation time. In fact, the ratio between the computation time of $\mathscr{C}_{LMC}$ and LLE for each phase diagram is almost five times faster when LLE is computed for a time of $\tau = 2^{15}$, whereas it is 174 times faster when $\tau = 2^{21}$. Let us remark since the LMC complexity indicator could be more accessible for experiments than the Lyapunov spectrum, which is more challenging to obtain. For completeness, we have also performed an analysis of the periodicities of the regular states using isospike diagrams, which reveal a rich structure in the space parameter. In addition, we have analyzed the influence of the initial conditions on the dynamical behavior for two different sets of parameters, finding bi-stability between a periodic and a chaotic state, and multistability among three regular states, respectively. In the near future, we will extend the study of complexity to other dynamical systems where the parameter space has been studied thoroughly from the Lyapunov exponents, as it is the case of magnetic systems.

Declaration of competing interest

The authors declare that they have no known competing financial interests or personal relationships that could have appeared to influence the work reported in this paper.

Data availability

No data was used for the research described in the article.

Acknowledgments

This manuscript is dedicated to Prof. Arecchi, who was an inspiring professor for the development of complex systems. LMP acknowledges the financial support from UTA-MAYOR 4725-22, Chile and from ANID, Chile through Convocatoria Nacional Subvención a Instalación en la Academia Convocatoria Año 2021, Grant SA77210040. DL, RMC, and SCS acknowledge the partial financial support from Centers of excellence with BASAL/ANID financing, Chile, Grant AFB220001, CEDENNA. Besides, DL acknowledges the hospitality of DIPC (Spain) where part of manuscript was written.

References

[1] Pathria RK, Beale P. Statistical mechanics. 3rd ed.. USA: Academic Press; 2011.
[2] Shannon CE. A mathematical theory of communication. Bell Syst Tech J 1948;27:379.
[3] Zwanzig R. Nonequilibrium statistical mechanics. UK: Oxford University Press; 2001.
[4] Prigogine I. Non-Equilibrium statistical mechanics. USA: Dover Publications; 2017.
[5] Kubo R, Toda M, Hashitsume N. Statistical physics II: Nonequilibrium statistical mechanics. Germany: Springer; 2012.
[6] López-Ruiz R, Mancini HL, Calbet X. A statistical measure of complexity. Phys Lett A 1995;209:321–6.
[7] Eckmann J-P, Ruelle D. Ergodic theory of chaos and strange attractors. Rev Modern Phys 1985;57:617–56.
[8] Bandt C, Pompe B. Permutation entropy: a natural complexity measure for time series. Phys Rev Lett 2002;88:174102.
[9] Rosso OA, Larrondo HA, Martin MT, Plastino A, Fuentes MA. Distinguishing noise from chaos. Phys Rev Lett 2007;99:154102.
[10] Bollt EM, Stanford T, Lai Y-C, Zyczkowski K. Validity of threshold-crossing analysis of symbolic dynamics from chaotic time series. Phys Rev Lett 2000;85:3524.
[11] Anteneodo C, Plastino AR. Some features of the Lopez-Ruiz–Mancini–Calbet (LMC) statistical measure of complexity. Phys Lett A 1996;223:348–54.
[12] Feldman DP, Crutchfield JP. Measures of statistical complexity: Why? Phys Lett A 1998;238:244–52.
[13] Calbet X, López-Ruiz R. Tendency towards maximum complexity in a nonequilibrium isolated system. Phys Rev E 2001;63:066116.
[14] Catalan RG, Garay J, López-Ruiz R. Features of the extension of a statistical measure of complexity to continuous systems. Phys Rev E 2002;66:011102.
[15] Batle J, Casas M, Plastino A, Plastino AR. Werner states and the two-spinors heisenberg anti-ferromagnet. Phys Lett A 2005;343:12–9.
[16] López-Ruiz R. Shannon information, LMC complexity and rényi entropies: a straightforward approach. Biophys Chem 2005;115:215.
[17] Lovallo M, Lapenna V, Telesca L. Transition matrix analysis of earthquake magnitude sequences. Chaos Solitons Fractals 2005;24:33–43.
[18] Martin MT, Plastino A, Rosso OA. Generalized statistical complexity measures: Geometrical and analytical properties. Phys A: Stat Mech Appl 2006;369:439–62.
[19] Rosso OA, Masoller C. Detecting and quantifying stochastic and coherence resonances via information-theory complexity measurements. Phys Rev E 2009;79:040106.
[20] Rosso OA, Masoller C. Detecting and quantifying temporal correlations in stochastic resonance via information theory measures. Eur Phys J B 2009;69:37–43.
[21] Ferri GL, Pennini I, Plastino A. LMC-complexity and various chaotic regimes. Phys Lett A 2009;373:2210–4.
[22] de Avellar MGB, Horvath JE. Entropy, complexity and disequilibrium in compact stars. Phys Lett A 2012;376:1085–9.
[23] Godó B, Nagy Á. Generalized complexity measures and chaotic maps. Chaos 2012;22:023118.
[24] Godó B, Nagy Á. Detecting regular and chaotic behaviour in the parameter space by generalised statistical complexity measures. Chaos Solitons Fractals 2015;78:26–32.
[25] Wiedermann M, Donges JF, Kurths J, Donner RV. Mapping and discrimination of networks in the complexity-entropy plane. Phys Rev E 2017;96:042304.
[26] Herrera L. New definition of complexity for self-gravitating fluid distributions: The spherically symmetric, static case. Phys Rev D 2018;97:044010.
[27] Mukherjee N, Roy AK. Some complexity measures in confined isotropic harmonic oscillator. J Math Chem 2019;57:1806.
[28] Wang Z, Shang P. Generalized entropy plane based on multiscale weighted multivariate dispersion entropy for financial time series. Chaos Solitons Fractals 2021;142:110473.
[29] Sharif M, Hassan K. Complexity factor for static cylindrical objects in f(G, T) gravity. Chinese J Phys 2022;77:1479.
[30] Pessa AAB, Zola RS, Perc M, Ribeiro HV. Determining liquid crystal properties with ordinal networks and machine learning. Chaos Solitons Fractals 2022;154:111607.
[31] Chacón M, Rojas-Pescio H, Peñaloza S, Landerretche J. Machine learning models and statistical complexity to analyze the effects of posture on cerebral hemodynamics. Entropy 2022;24:428.
[32] Amigó JM, Dale R, Tempesta P. Complexity-based permutation entropies: From deterministic time series to white noise. Commun Nonlinear Sci Numer Simul 2022;105:106077.
[33] Sambas A, Vaidyanathan S, Tlelo-Cuautle E, Abd-El-Atty B, Ahmed El-Latif A, Guillén-Fernández O, Sukono, Hidayat, Gundara G. A 3-D multi-stable system with a peanut-shaped equilibrium curve: Circuit design, FPGA realization, and an application to image encryption. IEEE Access 2020;8:137116.
[34] Vaidyanathan S, Shaobo H, Sambas A. A new multistable double-scroll 4-D hyperchaotic system with no equilibrium point, its bifurcation analysis, synchronization and circuit design. Arch Control Sci 2021;31:99.
[35] Oldroyd JG. On the formulation of rheological equations of state. Proc Roy Soc A 1950;200:523.
[36] Coleman BD, Noll W. Foundations of linear viscoelasticity. Rev Modern Phys 1961;33:239.
[37] Giesekus H. Die elastizitat von flussigkeiten. Rheol Acta 1966;5:29.
[38] Bird RB, Armstrong RC, Hassager O. Dynamics of polymeric liquids. vol. 1. New York: John Wiley & Sons; 1977.
[39] Larson RG. Constitutive equations for polymer melts and solutions. Boston: Butterworths; 1988.
[40] Pleiner H, Liu M, Brand HR. Nonlinear fluid dynamics description of nonNewtonian fluids. Rheol Acta 2004;43:502.
[41] Laroze D, Pleiner H. Thermal convection in a nonlinear non-newtonian magnetic fluid. Commun Nonlinear Sci Numer Simul 2015;26:167.
[42] Pérez LM, Bragard J, Díaz P, Mancini HL, Laroze D, Pleiner H. Magneto-viscous effect on thermal convection thresholds in an oldroyd magnetic fluid. J Magn Magn Mater 2017;444:432.
[43] Pérez LM, Bragard J, Laroze D, Martinez-Mardones J, Pleiner H. Thermal convection thresholds in an oldroyd magnetic fluid. J Magn Magn Mater 2011;323:691.
[44] Sharma RC. Effect of rotation on thermal instability of a viscoelastic fluid. Acta Phys Hung 1976;40:11.
[45] Khayat RE. Non-linear overstability in the thermal convection of viscoelastic fluids. J Non-Newton Fluid Mech 1994;53:331.
[46] Khayat RE. Chaos and overstability in the thermal convection of viscoelastic fluids. J Non-Newton Fluid Mech 1995;53:227.
[47] Abu-Ramadan E, Hay JM, Khayat RE. Characterization of chaotic thermal convection of viscoelastic fluids. J Non-Newton Fluid Mech 2003;115:79.
[48] Kolodner P. Oscillatory convection in viscoelastic DNA suspensions. J Non-Newton Fluid Mech 1998;75:167.
[49] Bear J. Modeling phenomena of flow and transport in porous media. Switzerland: Springer International Publishing AG; 2018.
[50] Sharma RC, Sunil. Thermal instability of an oldroydian fluid with suspended particles in hydromagnetics in porous medium. Polym Plast Technol Eng 1994;33:323.
[51] Sheu LJ, Tam LM, Chen JH, Chen HK, Lin KT, Kang Y. Chaotic convection of viscoelastic fluids in porous media. Chaos Solitons Fractals 2008;37:113.
[52] Bhadauria BS. Chaotic convection in a viscoelastic fluid saturated porous medium with a heat source. J Appl Math 2016;2016:1487616.
[53] Pyragas K. Continuous control of chaos by self-controlling feedback. Phys Lett A 1992;170:421.
[54] Yau HT, Chen CL. Chaos control of lorenz systems using adaptive controller with input saturation. Chaos Solitons Fractals 2007;34:1567.
[55] Pyragas K. Delayed feedback control of chaos. Philos Trans R Soc A 2006;364:2309.
[56] Mahmud MN, Siri Z, Vélez JA, Pérez LM, Laroze D. Chaotic convection in an oldroyd viscoelastic fluid in saturated porous medium with feedback control. Chaos 2020;30:073109.
[57] Lorenz EN. Deterministic nonperiodic flow. J Atmos Sci 1963;20:130.
[58] Sparrow C. The Lorenz equations: Bifurcations, chaos, and strange attractors. 2nd ed.. Germany: Springer; 1982.
[59] Roslan R, Mahmud MN, Hashim I. Effects of feedback control on chaotic convection in fluid-saturated porous media. Int J Heat Mass Transfer 2011;54:404.
[60] Clerc M, Coullet P, Tirapegui E. Lorenz bifurcation: Instabilities in quasireversible systems. Phy Rev Lett 1999;83(19):3820.
[61] Wolf A, Swift JB, Swinney HL, Vastano JA. Determining Lyapunov exponents from a time series. Phys D: Nonlinear Phenom 1985;16:285.
[62] Sprott JC. Chaos and time-series analysis. UK: Oxford University Press; 2003.

[63] Boccaletti S, Grebogi C, Lai YC, Mancini H, Maza D. The control of chaos: theory and applications. Phys Rep 2000;329:103–97.
[64] Rössler OE. An equation for hyperchaos. Phys Lett A 1979;71:155.
[65] Jia Q. Hyperchaos generated from the lorenz chaotic system and its control. Phys Lett A 2007;366:217.
[66] Vidal G, Mancini HL. Hyperchaotic synchronization under square symmetry. Int J Bifurc Chaos 2009;19:719–26.
[67] Urzagasti D, Becerra-Alonso D, Pérez LM, Mancini HL, Laroze D. Hyperchaotic magnetisation dynamics of two interacting dipoles. J Low Temp Phys 2015;181:211.
[68] Pikovsky A, Politi A. Lyapunov exponents: A tool to explore complex dynamics. Cambridge U. Press; 2016.
[69] Kantz H, Schreiber T. Nonlinear time series analysis. Cambridge U. Press; 2010.
[70] Boccaletti S, Bragard J, Arecchi FT, Mancini H. Synchronization in nonidentical extended systems. Phys Rev Lett 1999;83:536.
[71] Boccaletti S, Kurths J, Osipov G, Valladares DL, Zhou CS. The synchronization of chaotic systems. Phys Rep 2002;366:1–2.
[72] Gallas JAC. The structure of infinite periodic and chaotic hub cascades in phase diagrams of simple autonomous flows. Int J Bifurcation Chaos 2010;20:197.
[73] Zou Y, Thiel M, Romano MC, Kurths J. Shrimp structure and associated dynamics in parametrically excited oscillators. Int J Bifurc Chaos 2006;16:3567–79.
[74] Dullin HR, Schmidt S, Richter PH, Grossmann SK. Extended phase diagram of the lorenz model. Int J Bifurc Chaos 2007;17:3013–33.
[75] Barrio R, Blesa F, Serrano S. Topological changes in periodicity hubs of dissipative systems. Phy Rev Lett 2012;108:214102.
[76] Xing T, Barrio R, Shilnikov A. Symbolic quest into homoclinic chaos. Int J Bifurc Chaos 2014;24:1440004.
[77] Barrio R, Martínez MÁ, Serrano S, Wilczak D. When chaos meets hyperchaos: 4D rössler model. Phys Lett A 2015;379:2300–5.
[78] Façanha W, Oldeman B, Glass L. Bifurcation structures in two-dimensional maps: The endoskeletons of shrimps. Phys Lett A 2013;377:1264–8.
[79] Pérez LM, Bragard J, Mancini HL, Gallas JAC, Cabanas AM, Suarez OJ, Laroze D. Effect of anisotropy on magnetization dynamics. Netw Heterog Media 2015;10:209.
[80] Laroze D, Bragard J, Suarez OJ, Pleiner H. Characterization of the chaotic magnetic particle dynamics. IEEE Trans Magn 2011;47:3032.
[81] Bragard J, Pleiner H, Suarez OJ, Vargas P, Gallas JAC, Laroze D. Chaotic dynamics of a magnetic nanoparticle. Phys Rev E 2011;84:037202.
[82] Laroze D, Becerra-Alonso D, Gallas JAC, Pleiner H. Magnetization dynamics under a quasiperiodic magnetic field. IEEE Trans Magn 2012;48:3567.
[83] Cabanas AM, Pérez LM, Laroze D. Strange non-chaotic attractors in spin valve systems. J Magn Magn Mater 2018;460:320–6.
[84] Vélez JA, Bragard J, Pérez LM, Cabanas AM, Suarez OJ, Laroze D, Mancini HL. Periodicity characterization of the nonlinear magnetization dynamics. Chaos 2020;30:093112.
[85] Cabanas AM, Vélez JA, Pérez LM, Díaz P, Clerc MG, Laroze D, Malomed BA. Dissipative structures in a parametrically driven dissipative lattice: Chimera, localized disorder, continuous-wave, and staggered states. Chaos Solitons Fractals 2021;146:110880.
[86] Cabanas AM, Rivas R, Pérez LM, Vélez J, Díaz P, Clerc MG, Pleiner H, Laroze D, Malomed BA. A quasi-periodic route to chaos in a parametrically driven nonlinear medium. Chaos Solitons Fractals 2021;151:111089.
[87] Kanchana C, Vélez JA, Pérez LM, Laroze D, Siddheshwari PG. Influence of higher-order modes on ferroconvection. Chaos 2022;32:083129.
[88] Kanchana C, Siddheshwar PG, Pérez LM, Laroze D. Comparison of the effect of suction-injection-combination on Rayleigh–Bénard convection in the case of asymmetric boundaries with those of symmetric ones. Phys Fluids 2023;35:053615.
[89] Nascimento MA, Gallas JA, Varela H. Self-organized distribution of periodicity and chaos in an electrochemical oscillator. Phys Chem Chem Phys 2011;13:349–784.
[90] Freire JG, Gallas JAC. Stern–brocot trees in the periodicity of mixed-mode oscillations. Phys Chem Chem Phys 2011;13:12191.
[91] Gallas MR, Gallas MR, Gallas JAC. Distribution of chaos and periodic spikes in a three-cell population model of cancer. Eur Phys J: Spec Top 2014;223:2131–44.
[92] Sack A, Freire JG, Lindberg E, Pöschel T, Gallas JAC. Discontinuous spirals of stable periodic oscillations. Sci Rep 2013;3:3350.
[93] Park J, Lee H, Jeon Y, Baik J. Periodicity of the lorenz-stenflo equations. Phys Scr 2015;90:065201.
[94] Park J, Lee H, Baik J. Periodic and chaotic dynamics of the ehrhard-müller system. Int J Bif Chaos 2016;26:1630015.
[95] Gallas JAC. Spiking systematics in some CO2 laser models. Adv At, Mol, Opt Phys 2016;65:127–91.
[96] Moon S, Han B, Park J, Seo JM, Baik J. Periodicity and chaos of high-order lorenz systems. Int J Bifur Chaos 2017;27:1750176.
[97] Wiggers V, Rech PC. Multistability and organization of periodicity in a van der pol-duffing oscillator. Chaos, Solit Fractals 2017;103:632–7.
[98] Wiggers V, Rech PC. Chaos, periodicity, and quasiperiodicity in a radio-physical oscillator. Int J Bifur Chaos 2017;27:1730023.
[99] Rech PC. Organization of the periodicity in the parameter-space of a glycolysis discrete-time mathematical model. J Math Chem 2019;57:632–7.
[100] Rech PC, Dhua S, Pati NC. Multistability and bubbling route to chaos in a deterministic model for geomagnetic field reversals. Int J Bifur Chaos 2019;29:1930034.
[101] Gallas JA. Stability diagrams for a memristor oscillator. Eur Phy J Spe Top 2019;228:2081.
[102] Moon S, Han B, Park J, Seo J, Baik J. A physically extended lorenz system. Chaos 2019;29:063129.
[103] Freire JG, Caldeórn A, Varela H, Gallas JA. Phase diagrams and dynamical evolution of the triple-pathway electro-oxidation of formic acid on platinum. Phys Chem Chem Phys 2020;22:1078–91.
[104] Volos CK, Gallas JA. Experimental evidence of quint points and non-quantum chirality in a minimalist autonomous electronic oscillator. Eur Phys J Plus 2022;137:154.
[105] Bayani A, Rajagopal K, Khalaf AJM, Jafari S, Leutcho GD, Kengne J. Dynamical analysis of a new multistable chaotic system with hidden attractor: Antimonotonicity, coexisting, multiple attractors, and offset boosting. Phys Lett A 2019;383:1450–6.
[106] Wei Z, Pham V-T, Khalaf AJM, Kengne J, Jafari S. A modified multistable chaotic oscillator. I Int J Bifur Chaos 2018;28:1850085.
[107] Pisarchik AN, Feudel U. Control of multistability. Phys Rep 2014;540:167–218.
[108] Dudkowski D, Jafari S, Kapitaniak T, Kuznetsov NV, Leonov GA, Prasad A. Hidden attractors in dynamical systems. Phys Rep 2016;637:1–50.
[109] Jafari S, Sprott JC, Nazarimehr F. Recent new examples of hidden attractors. Eur Phys J Spec Top 2015;224:1469–76.
[110] Siddheshwar PG, Kanchana C, Laroze D. A study of Darcy-Bénard regular and chaotic convection using a new local thermal non-equilibrium formulation. Phys Fluids 2021;33:044107.
[111] Munmuangsaen B, Srisuchinwong B. A hidden chaotic attractor in the classical lorenz system. Chaos Solitons Fractals 2018;107:61–6.